Power Flow Control in Multi-Active-Bridge Converters: Theories and Applications

Yenan Chen*, Ping Wang*, Haoran Li† and Minjie Chen*
Email: {yenanc, pwang2, minjie}@princeton.edu; hr-li15@mails.tsinghua.edu.cn
*Princeton University, Princeton, NJ 08540, USA
†Tsinghua University, Beijing, 100086, China

***Abstract*—This paper investigates the theories and applications of power flow control in multi-active-bridge (MAB) power converters. Many emerging applications including differential power processing, low voltage power delivery in smart homes, multi-cell battery balancers, and photovoltaic energy systems comprise sophisticated power flow across multiple dc voltage ports. Connecting many dc voltage ports together with a MAB converter reduces the power conversion stress, improves the efficiency and enhances the power density. Fundamentally, the advantages of a MAB design come from merging many standalone magnetic components with simple functions into one single magnetic component that performs sophisticated functions. Three control strategies for MAB converters, including phase-shift (PS) control, time-sharing (TS) control, and hybrid phase-shift and time-sharing (PSTS) control are developed to regulate the voltage and precisely control the power flow. A four-port MAB converter prototype designed for low voltage power delivery applications in future smart homes has been built and tested to compare the performance of the three control methods and verify the effectiveness of the proposed architecture.**

***Index Terms*—dc power delivery, multi-active-bridge converter, power flow control, multiwinding transformer, planar magnetics.**

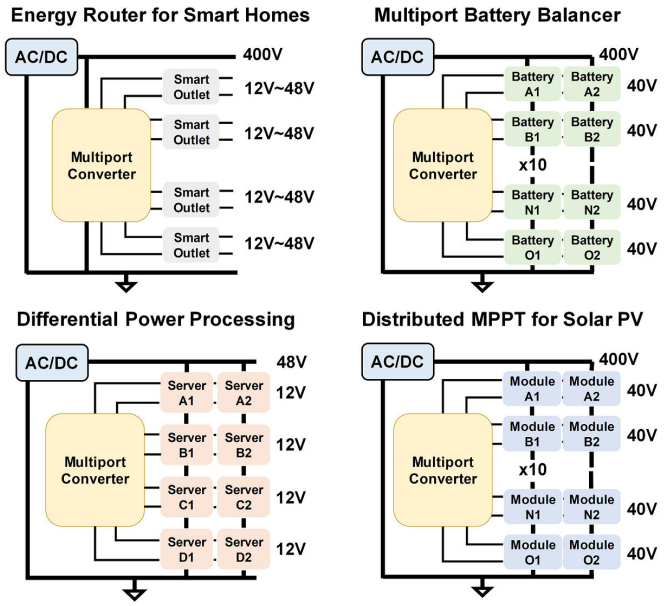

Fig. 1. Four application scenarios of multiport power converters: 1) dc energy router for smart homes; 2) multiport battery balancer for grid scale energy storage; 3) differential power processor architecture for series stacked servers; and 4) distributed MPPT for solar photovoltaic systems.

I. Introduction

Traditionally, power converters are usually designed as single-input single-output converters. For battery energy storage, server racks, and PV strings, a large number of modular cells need to be connected in series and/or parallel and need be coordinated to achieve maximum system performance. In future homes and buildings, more and more devices operate in low voltage dc, have battery storage, and can provide grid support functions. Power converters that can interface with multiple dc voltage domains with high efficiency and high power density are needed in a wide range of applications. Fig. 1 shows the power conversion architecture in four future application scenarios which all need multiport power converters with sophisticated power flow, including 1) energy router for smart homes; 2) multiport battery balancer; 3) differential power processing for series-stacked servers; and 4) distributed MPPT for solar photovoltaic systems.

Multi-active-bridge (MAB) converter is a family of power converters with many inverter bridges (half-bridges or full-bridges) coupled to a single multi-winding transformer. Fig. 2 shows an example 4-port MAB topology with four full bridge active ports connected to a 4-winding transformer. The voltage of the four dc voltage ports are 400V, 48V, 15V and 5V, respectively. MAB topologies are nature expansions of the well-known dual-active-bridge (DAB) family [1], [2]. MAB converters have been adopted in energy router, solid state transformer and electric vehicle applications [3]–[5]. It is preferable to implement the multi-winding transformer as a planar single-core structure with printed-circuit-board (PCB) windings to improve the efficiency and increase the power density [6]–[8]. One key challenge in MAB design is the the cross-coupling of the matrix power flow in the multi-winding transformer. The matrix power flow in a MAB converter can be controlled by implementing a PI controller at each of the dc voltage port [9]. The PI controller senses the voltage at each port and adjusts the phases of the inverter bridges accordingly to regulate the voltage. [10] proposes a power flow decoupling method with the assumption that the converter operates with very small phase-shift across multiple ports. The power flow in the multi-winding transformer of a MAB architecture can be treated in the same way as controlling the power flow in a traditional 60 Hz ac grid, except that the system operates at a frequency that is much higher than 60 Hz. Each port functions

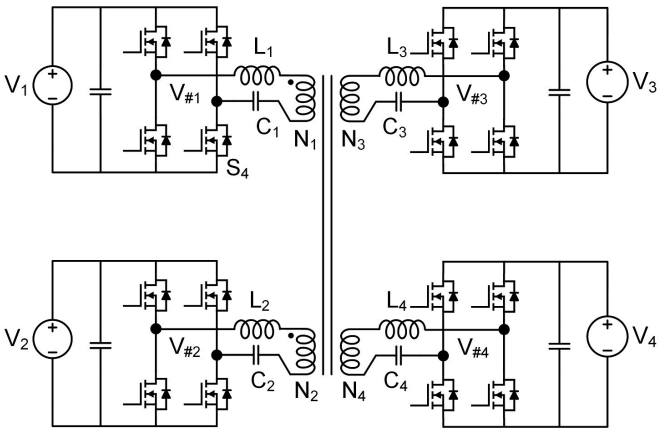

Fig. 2. Topology of an example 4-port MAB converter.

as a controllable voltage source, which behaves similarly as synchronous generators in a traditional power system. Newton-Raphson algorithm was used in [11], [12] to solve the phase-shift angle at each port for a given power flow.

Another method to route the matrix power flow in a MAB converter is time-sharing (TS) control (on-off control) [13]. At each time instance, only two ports are activated and power flows from one to the other. At a result, the MAB converter can be treated as a two-port DAB converter with no cross-coupling across multiple ports. Similar to bursting a single-input single-output converter, time-sharing control enables the system to achieve high efficiency in light load conditions, and reduce the system efficiency in heavy load conditions. As will be discussed in Section IV, time-sharing control can be merged with phase-shift control to create mutual system advantages.

This paper uses a MAB converter designed for low voltage dc power delivery applications as an example to investigate the theories and applications of power flow control in multi-port converters. Compared to a traditional dc power delivery architecture with a fixed dc bus (usually 400 V), a MAB design can eliminate the numerous dc-dc adapters, reduce the power conversion stress, and improve the power density. The conventional dc-dc adapters attached to each low voltage devices will be replaced by a central MAB converter (located at the circuit box of a room or a building) that can create many adjustable dc voltage levels for many smart outlets. A smart outlet has communication and voltage regulation capability. It senses the type of the load, and communicates with the controller of the MAB to synthesize the needed voltage.

The remainder of this paper is organized as follows: Section II presents the operation principles of phase-shift control. Section III presents the operation principles of time-sharing control. Section IV investigates a hybrid phase-shift time-sharing control. The design details of a 400 W MAB converter are presented in Section V and the small signal analysis are presented in Section VI. Section VII discusses the experimental results. Finally, Section VIII concludes the paper.

II. Phase-Shift Control of the Power Flow

In the topology shown in Fig. 2, Port #1 connects the MAB converter to a 400V dc bus synthesized by a central ac-dc converter. Port #2 is designed to charge and discharge a battery system at 48V. Port #3 and Port #4 deliver power to low voltage consumer electronics (e.g., cellphones and laptops) at 15V and 5V, respectively. N_1–N_4 are the number of turns of the multi-winding transformer. Branch inductors L_1–L_4 represent the summation of the leakage inductance of the transformer and external discrete inductors. Depending on the leakage inductance and the switching frequency, external inductors may or may not be needed. In a MAB implementation, the impedance of the dc blocking capacitors, C_1–C_4, are negligible compared to the impedance of L_1–L_4.

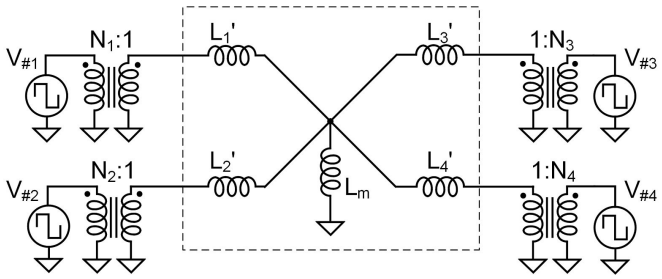

Fig. 3. Star model of a multi-winding transformer.

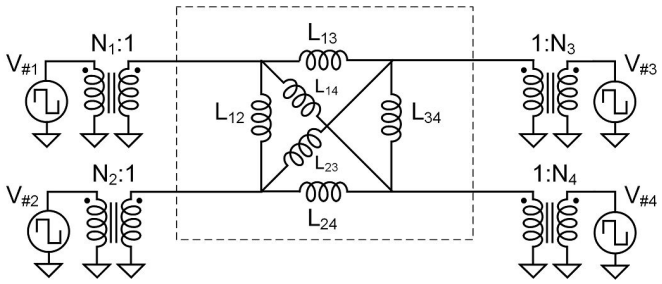

Fig. 4. Delta model of a multi-winding transformer.

A. Power Flow Modulation and Large Signal Models

The multi-winding transformer in this 4-port MAB converter can be represented as a Star model (Fig. 3). The Star model can be converted into an equivalent Delta model [4] (Fig. 4) or a Cantilever model [14] to simplify the power flow analysis. The four full-bridge inverters are modeled as four square wave voltage sources $V_{\#1}$–$V_{\#4}$. An N turn winding in the multi-winding transformer is represented as an ideal transformer with a turns ratio of $N:1$. The series-connected capacitors C_1–C_4 are neglected in this analysis. A power flow calculation method considering the impact of these capacitors is provided in [11]. The equivalent inductance between Port #i and Port #j in the Delta model can be calculated as a function of the equivalant port inductance in the Star model:

$$L_{ij} = L_i' L_j' \left(\frac{1}{L_m} + \sum_{k=1}^{4} \frac{1}{L_k'} \right), \tag{1}$$

where L_1'–L_4' are the normalized inductance per-turn of L_1–L_4 in the Star model (e.g. $L_i' = L_i/N_i^2$). L_m is the magnetizing inductance.

As derived in [11], the average injected power from the transformer in one switching cycle at Port #i is:

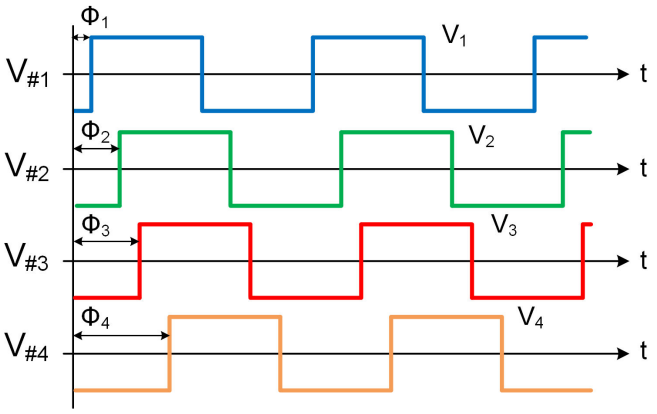

Fig. 5. Phase-shift modulation of the 4-port MAB converter. The phases from Port #1 to Port #4 are Φ_1 to Φ_4, respectively.

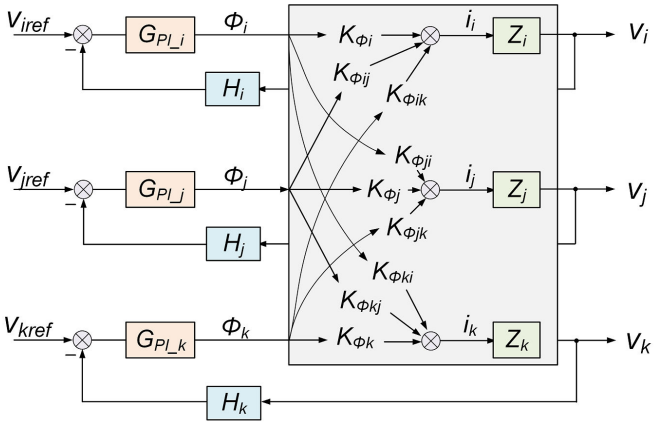

Fig. 6. Diagram of the voltage regulation control loop. The voltage of each port is modulated by a PI controller which adjusts the phase of this port.

$$P_i = \frac{V_i}{2\pi f_s N_i} \sum_{j \neq i} \frac{V_j}{N_j L_{ij}} (\Phi_i - \Phi_j) \left(1 - \frac{|\Phi_i - \Phi_j|}{\pi}\right). \quad (2)$$

Here V_i, V_j are the voltage of Port #i and Port #j; f_s is the switching frequency; and Φ_i, Φ_j are the phase-shift angles of Port #i and Port #j shown in Fig. 5. Usually Port #1 is set as the reference port and its phase Φ_1 is zero.

A Newton-Raphson solver is developed in [11] to iteratively find the corresponding phase $[\Phi_1, ..., \Phi_n]$ for a given power flow matrix $[P_1, ..., P_n]$. If $[P_1, ..., P_n]$ is a feasible power flow and if the multi-winding transformer is closely coupled, the Newton-Raphson method usually converges to the correct phase solution within a few steps.

B. Port Voltage Regulation and Small Signal Models

Port voltage regulation is needed if the MAB converter is loaded with resistive loads or current-source-behaviored loads. Based on (2), the dc voltage across Port #i is:

$$V_i = \frac{R_i}{2\pi f_s N_i} \sum_{j \neq i} \frac{V_j}{N_j L_{ij}} (\Phi_i - \Phi_j) \left(1 - \frac{|\Phi_i - \Phi_j|}{\pi}\right). \quad (3)$$

Here R_i is the equivalent resistance of the load. The small signal transfer function from perturbations in the phase-shift angle of each port $[\phi_1, ..., \phi_n]$ to the voltage of Port #i is:

$$\begin{aligned} \hat{v}_i = Z_i \times \hat{i}_i &= \frac{R_i}{sR_iC_i + 1} \times \frac{1}{2\pi f_s N_i} \\ &\times \left[\hat{\phi}_i \sum_{j \neq i} \frac{V_j}{N_j L_{ij}} \left(1 - \frac{2|\Phi_i - \Phi_j|}{\pi}\right) \right. \\ &\left. - \sum_{j \neq i} \hat{\phi}_j \frac{V_j}{N_j L_{ij}} \left(1 - \frac{2|\Phi_i - \Phi_j|}{\pi}\right)\right] \\ &= (K_{\phi i}\hat{\phi}_i + \sum_{j \neq i} K_{\phi ij}\hat{\phi}_j) \times Z_i \\ &= G_{\phi vi}\hat{\phi}_i + \sum_{j \neq i} G_{\phi vij}\hat{\phi}_j, \end{aligned} \quad (4)$$

where C_i is the bus capacitance of port #i. Fig. 6 shows the small signal model of the MAB converter. Note that all the control loops are cross coupled with the phase to current transfer function $K_{\Phi i}$ and the port load impedance Z_i. The small signal dynamic behaviors of the system will be analyzed in detail in Section V.

C. Split Power Point Tracking (SPPT)

The power flow needs to be precisely merged or splitted among multiple ports in many applications. A *Split Power Point Tracking (SPPT)* algorithm, which is similar to the *Maximum Power Point Tracking (MPPT)* algorithm in photovoltaic systems, is needed in the control loop to determine the power splitting ratio. Based on (2), if the phase difference between two ports is smaller than $\pi/2$, the power transferred from one port to the other is monotonically determined by the phase difference – a larger phase difference pushes more power from the leading ports to the lagging ports. One can delay the phase of Port #i and maintain all other phases the if more power needs to be delivered to Port #i. Using the 4-port MAB converter shown in Fig. 2 as an example, assuming the phase of Port #1 is zero, Port #1 and Port #2 are input ports, and Port #3 and Port #3 are output ports. The total input power is $P_1 + P_2$, and the total output power is $P_3 + P_4$. Fig. 7 shows the control diagram if one wants to feed $K(P_3 + P_4)$ from Port #2, and $(1 - K)(P_3 + P_4)$ from Port #1. K is the power dividing ratio between P_1 and P_2, ΔP is a hysteresis margin to avoid oscillation. $\Delta\Phi$ is the incremental phase step. Φ_2 is increased or reduced by $\Delta\Phi$ in every tracking step until the difference between P_2 and its control target $K(P_3 + P_4)$ is smaller than ΔP.

For a MAB system with many input ports and output ports, the power combining and splitting ratios are multi-variable vectors and are cross-coupled. A multi-variable SPPT algorithm which can systematically track many splitting ratios is an interesting topic and is beyond the scope of this paper.

III. Time-Sharing Control of the Power Flow

Another method to control the power flow in a MAB converter is time-sharing control. With time-sharing control, only two ports are activated at one instance; all other ports are

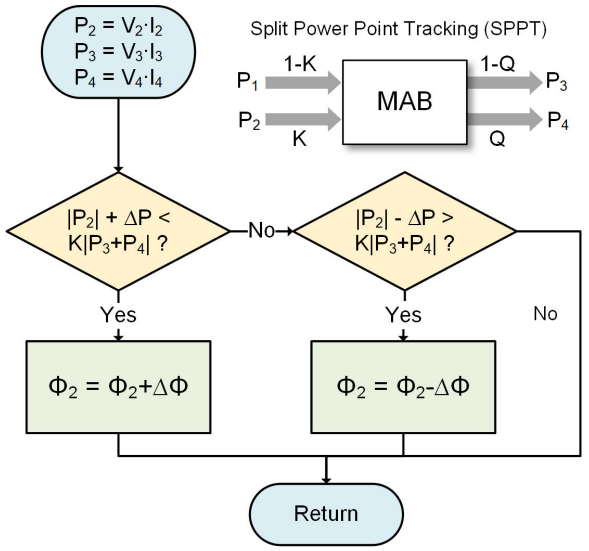

Fig. 7. Split power point tracking of MAB converters. This diagram shows a SPPT tracking algorithm to modulate the phase of Port #2 while keeping the phases of all other ports fixed.

deactivated as diode rectifiers. With time-sharing control, the MAB converter functions as a DAB converter with a single input port, a single output port with straight-forward power flow. Fig. 8 illustrates the principles of time-sharing control, when Port #1 delivers power to Port #2 during D_2, delivers power to Port #3 during D_3, and delivers power to Port #4 during D_4. The time-sharing period is T_m, which is much longer than the switching period T_s. D_2–D_4 are the time-sharing ratios and $D_2 + D_3 + D_4 \leq 1$. The instantanious power delivered in D_2–D_4 may or may not be the same. With time-sharing control, the average port power in one switching cycle when the port is activated is:

$$P_i = \frac{V_1 V_i \Phi_i (\pi - |\Phi_i|)}{2\pi^2 f_s N_1 N_i (L_1' + L_i')}. \tag{5}$$

The average port power in one time-sharing period is:

$$\langle P_i \rangle_{T_m} = D_i P_i = D_i \frac{V_1 V_i \Phi_i (\pi - |\Phi_i|)}{2\pi^2 f_s N_1 N_i (L_1' + L_i')}. \tag{6}$$

Fixing all phase angles and use the time-sharing duty cycle as the only control variables, the transfer function from the time-sharing duty ratio to the port voltage is:

$$\hat{v}_i = \frac{V_1 \Phi_i (\pi - |\Phi_i|)}{2\pi^2 f_s N_1 N_i (L_1' + L_i')} \frac{R_i}{sR_iC_i + 1} \hat{d}_i = G_{dvi} \hat{d}_i. \tag{7}$$

Time-sharing control decouples the sophisticated power flow in a MAB system and greatly simplifies the control. The duty ratios of each period should be closely monitored to avoid operation overlapping. In fact, time-sharing control modulates the port voltage and power by adjusting the number of power pulses in one control period, which is similar to the Discrete Pulse Modulation (DPM) concept in dc-dc or grid-interface power converters.

Similary to burst-mode control, time-sharing control can be used to improve the efficiency of a MAB converter operating in light load. On the other hand, the maximum power rating of time-sharing control is usually limited by the time-sharing duty ratio. Time-sharing control also requires larger filtering capacitors at the ports. The discontinuous operation of the transformer may also make audible noise if the time-sharing modulation frequency locates in the audible range.

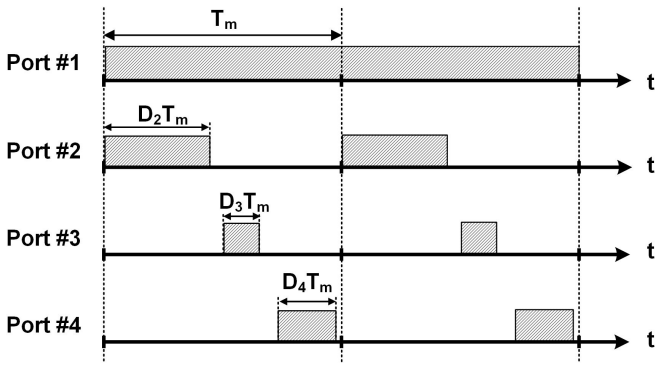

Fig. 8. Time-sharing control of the 4-port MAB converter. Port #1 is an input port and Port #2-4 are output ports.

IV. Hybrid Phase-Shift Time-Sharing Control

There is a fundamental tradeoff between time-sharing control and phase-shift control: time-sharing control decouples the complex power flow and is easy to implement, but the device stress and voltage ripple are usually higher; phase-shift control is sophisticated with cross-coupled power flow, but the power conversion stress and energy storage requirements are usually lower. To leverage the advantages of the two power flow methods, we explore the possibility of merging the two power flow control methods to create mutual advantages.

We use the following example to explain the principles of hybrid phase-shift time-sharing control. The MAB system is delivering power from Port #1 to Port #2–#4. D_3 and D_4 are modulated by time-sharing control with fixed phases Φ_3 and Φ_4. D_2 is set to be exactly $1 - D_3 - D_4$, and Φ_2 is determined by phase-shift control. The small signal model linking the phase of Port #2, ϕ_2 and the port ac voltage, v_2, is:

$$\hat{v}_2 = \frac{V_1 (\pi - 2|\Phi_2|)}{2\pi^2 f_s N_1 N_2 (L_1' + L_2')} \frac{R_2}{sR_2C_2 + 1} D_2 \hat{\phi}_2. \tag{8}$$

The voltage control loops of the three output ports are all decoupled with hybrid phase-shift time-sharing control. Hybrid phase-shift time-sharing control reduces the the instantaneous power of Port #1 and Port #2 during D_2 due to the extended operating period. The efficiencies of Port #1 and Port #2 are higher than phase-shift control, but not higher than time-sharing control. The efficiencies of Port #3 and Port #2 maintain the same. The low frequency voltage ripple of Port #2 is usually smaller than its voltage ripple with time-sharing control due to smaller energy buffering requirement on the filter capacitors. That audible noise also disappears because the transformer operates continuously in one time-sharing modulation cycle.

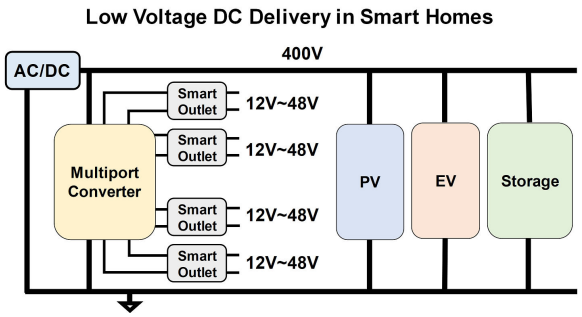

Fig. 9. A MAB converter for dc power delivery in smart homes.

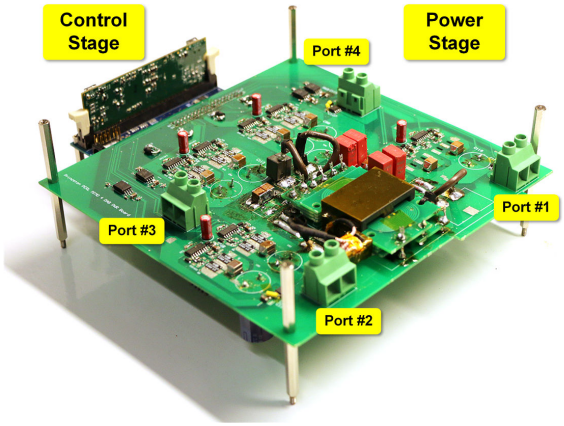

Fig. 10. Picture of the 4-port MAB converter.

V. Prototype Design

A prototype of 4-port MAB converter has been built and tested for dc power delivery in smart homes. As shown in Fig. 9, the MAB converter interface with a roof-top PV system at 400V, with a battery energy storage system at 48V, and provide 12V-48V voltage rails to home appliances. Fig. 10 shows a picture of this prototype. Table I lists the design details of this prototype. The rated power for Port #1–Port #4 are 400 W, 300 W, 150 W, and 75 W, respectively. The turn ratio of the transformer is 80:10:3:1. If all ports are in phase, the maximum flux density in the core, B_{max}, is:

$$B_{max} = \frac{V_1 T_s}{4 N_1 A_e}. \tag{9}$$

Here A_e is the effective area of the core, T_s is the switching period, and V_1/N_1 is the voltage per turn. The PCB transformer is implemented as a E38/8/25 core with 3F36 material. B_{max} is 64.4 mT at 100 kHz. The transformer windings are implemented as four vertically stacked 4-layer PCBs. The leakage inductance L_{lk1}–L_{lk4} are 18.2μH, 0.81μH, 84.1nH, 26.4nH, all measured at each port. The magnetizing inductance is 39.08 mH referred to Port #1. The maximum power that Port #i can carry is:

$$P_{imax} = \frac{V_i}{8 f_s N_i} \sum_{j \neq i} \frac{V_j}{N_j L_{ij}} \approx \frac{V_o^2}{8 f_s} \sum_{j \neq i} \frac{1}{L_{ij}}. \tag{10}$$

Here V_o is the voltage per turn. f_s is the switching frequency. V_o, f_s and L_{ij} should be carefully selected such that all ports can carry sufficient power. The MAB converter is controlled by a microcontroller (TI F28069 DSP).

TABLE I
Specifications and Parameters of the MAB Converter

Specifications & Symbol	Description
Rated Port Power: $P_1 - P_4$	400 W, 300 W, 150 W, 75 W
Rated Port Voltage: $V_1 - V_4$	400 V, 48 V, 15 V, 5 V
Switching Frequency: f_s	100 kHz
Port #1 Switches	GS66508T 650 V/30 A/50 mΩ
Port #2–#4 Switches	GS61008P 100 V/90 A/7 mΩ
Transformer	Ferroxcube E38/8/25, 3F36 80:10:3:1, 4×4-layer PCB
Leakage Inductance: $L_{lk1} - L_{lk4}$	18.2 μH, 0.81 μH 84.1 nH, 26.4 nH
Magnetizing Inductance: L_m	39.08 mH
External Inductors: $L_{ext1} - L_{ext4}$	0, 4.2 μH, 200 nH, 100 nH
Bus Capacitors: $C_1 - C_4$	120 μF, 2 mF, 20 mF, 40 mF
DC Blocking Capacitors: $C_{b1} - C_{b4}$	10 μF, 20 μF, 134 μF, 154 μF

The size of the filtering capacitor at each port is determined by the time-sharing control. The bus voltage ripple of each port in time-sharing control is:

$$\Delta v_i = \frac{P_i D_i (1 - D_i) T_m}{C_i V_i} \leq \frac{P_i T_m}{4 C_i V_i}. \tag{11}$$

Here V_i is the port voltage and T_m is the time-sharing period. With the parameters listed in Table I, for a time-sharing frequency of 1 kHz, the maximum voltage ripple ratio from Port #1 to Port #4 is 0.52%, 1.63%, 0.83%, and 1.875%, respectively.

VI. Small Signal Stability Analysis

With phase-shift control, based on Fig. 6 and (4), the small signal loop gain of the port voltage is:

$$G_{PSi}(s) = H_i(s) G_d(s) G_{\phi vi}(s). \tag{12}$$

Here H_i(s) is the transfer function of the voltage sampling circuit and $G_d(s)$ is the delay of the digital control circuitry. Fig. 11 shows the Bode plot of G_{PS2}(s). The phase-shift difference in $G_{\phi v2j}(s)$ is set as zero (no purtubation from other ports). The bandwidth of the original loop transfer function is 320 Hz with a phase margin of 26.4°. Fig. 11 shows the Bode plot of PI controller $G_{PI2}(s)$, with which the phase margin is improved to 84° and the bandwidth is decreased to 13.2 Hz.

With time-sharing control, based on (7), the small signal loop gain of the port voltage is:

$$G_{TSi}(s) = H_i(s) G_d(s) G_{dvi}(s). \tag{13}$$

Fig. 12 shows the Bode plot of Port #3 with time-sharing control. With a PI controller the bandwidth of the loop transfer function decreases from 650 Hz to 49 Hz while the phase margin increases from 14.2° to 66.8°.

With hybrid control, the voltage of Port #2 is still controlled by the phase-shift angle and its loop gain function is similar to (12). Comparing (4) with (8), we can find that the only

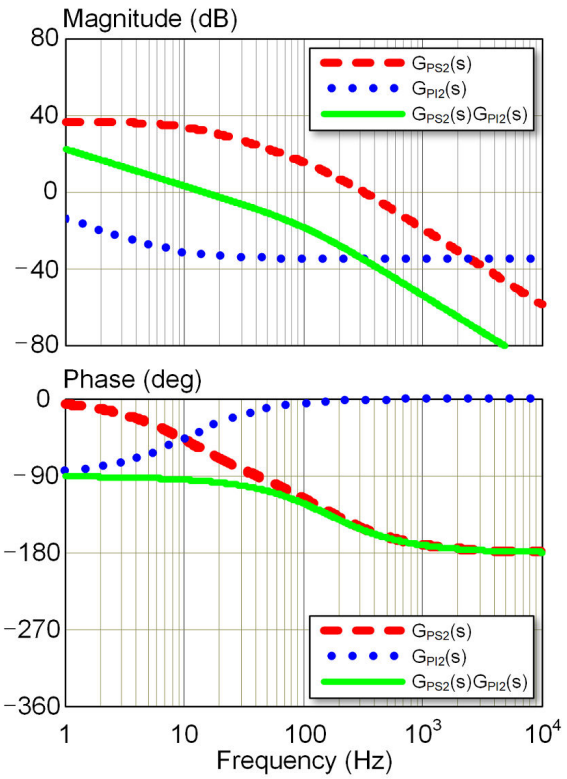

Fig. 11. Bode plots of the original loop gain function $G_{PS2}(s)$, the PI controller $G_{PI2}(s)$ and $G_{PS2}(s)G_{PI2}(s)$ with phase-shift control.

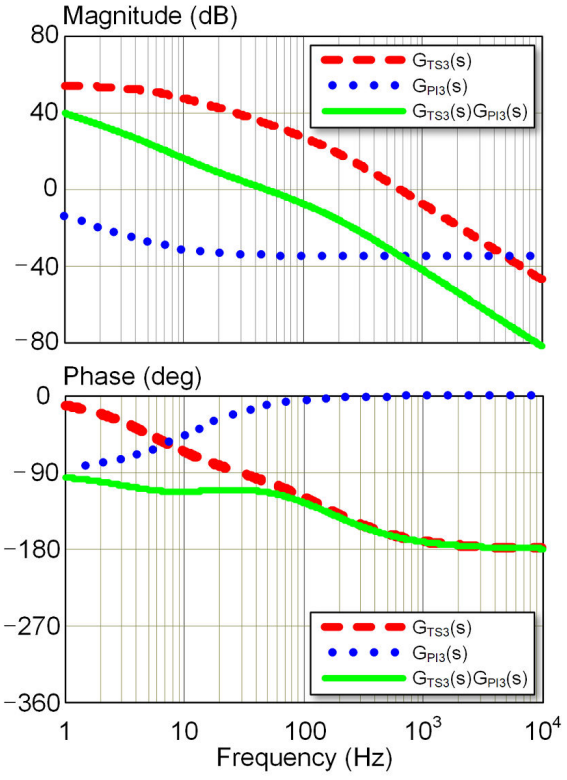

Fig. 12. Bode plots of the original loop gain function $G_{TS3}(s)$, the PI controller $G_{PI3}(s)$ and $G_{TS3}(s)G_{PI3}(s)$ with time-sharing control.

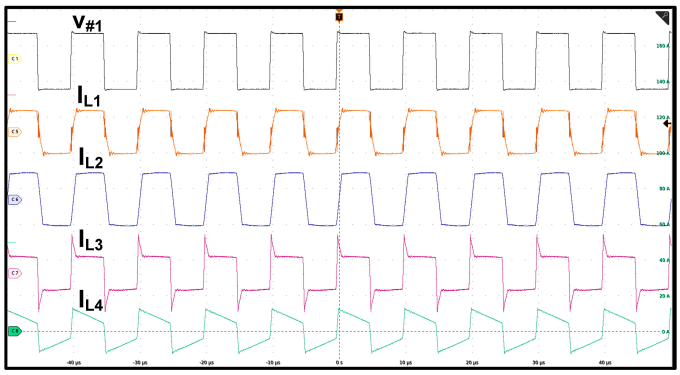

Fig. 13. Waveforms with phase-shift control: 400V input, 48V output at 300W, 15V output at 70W, 5V output at 35W.

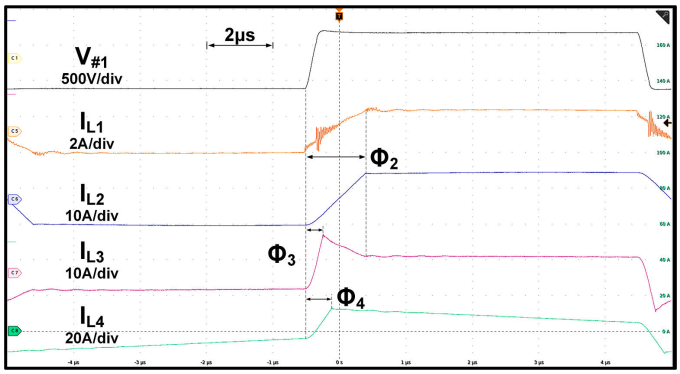

Fig. 14. Zoom-in waveforms with phase-shift control: 400V input, 48V output at 300W, 15V output at 70W, 5V output at 35W.

difference is the loop gain. The same PI controller is applied to Port #2 with both phase-shift control and hybrid control. As expected, the bandwidth and phase margin in both mode are almost the same with the two control methods.

VII. Experimental Results

The performance of the MAB prototype is measured across a variety of operating conditions. Fig. 13 shows the waveforms of ac input voltage of the 400V winding $V_{\#1}$ and the branch inductance current $I_{L1} - I_{L4}$ with phase-shift control. Fig. 14 shows the phase-shift angle of each port. Port #2–Port #4 achieved zero-voltage-switching (ZVS) at this operating point.

Fig. 15 show the measured waveform of the system with two input ports and two output ports. Fig. 16 shows the transient waveform with a step change in the power dividing ratio. The phase of each port is updated every 10 ms. Current spikes are observed on the waveform of I_{L1} in Fig. 15 due to hard-switching of the 400V port switches.

Two example cases of time-sharing control and hybrid control with a control cycle of 1 ms are presented in Fig. 17. The instantaneous power of Port #2–Port #4 with time-sharing control is 100 W, 100 W, 50 W respectively. The time-sharing duty ratio of Port #2–Port #4 can be found in the branch current waveforms, which is close to 60%, 10% and 20%. With hybrid control, the duty ratio of Port #2 is 70% and instantaneous power is approximately 85.7 W.

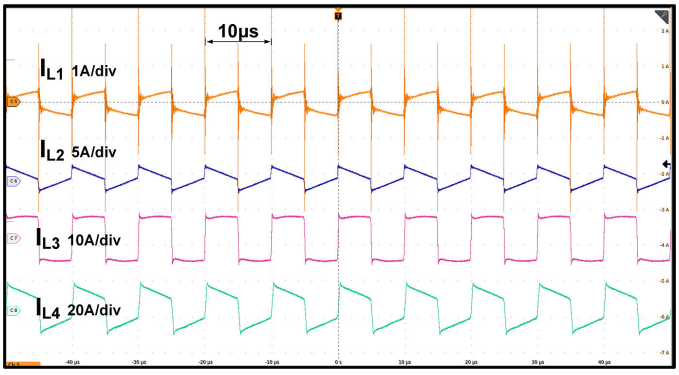

Fig. 15. Waveforms with phase-shift control: 400V input at 80W, 48V input at 40W, 15V output at 80W, 5V output at 40W.

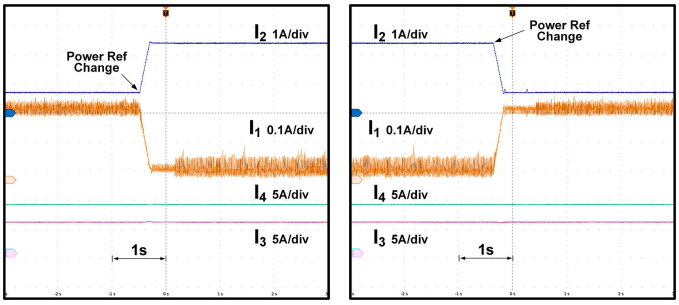

Fig. 16. Input power regulation with phase-shift control: 400V input change between 20W and 100W, 48V input change between 100W and 20W, 15V output at 75W, 5V output at 45W.

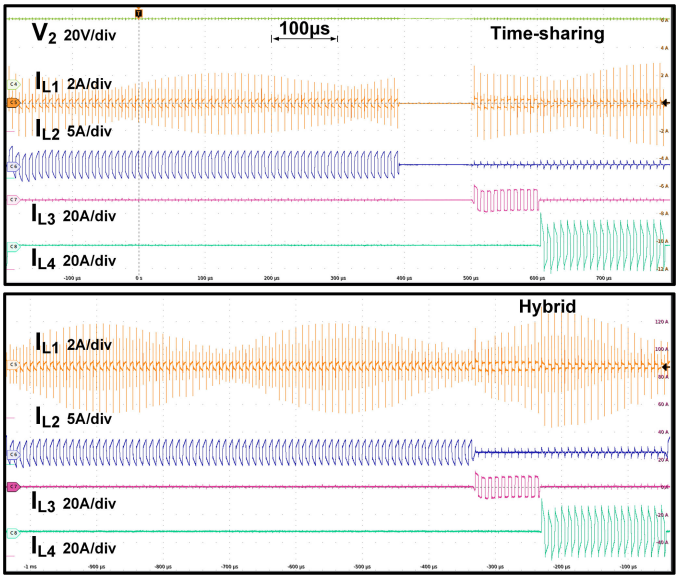

Fig. 17. Time-sharing and Hybrid control: 400V input, 48V output at 60W, 15V output at 10W, 5V output at 10W, control cycle is 1ms.

Fig. 18 shows the efficiency of the system with Port #1 as the input and Port #2–#4 as the output, individually one-at-a-time. The system operates as a DAB converter with one input and one output. The peak efficiency of 400 V–48 V operation is 98%. The peak efficiency of 400 V–15 V operation is 92%. The peak efficiency of 400 V–5 V operation is about 70%. The measured efficiency with DAB operation is used to select

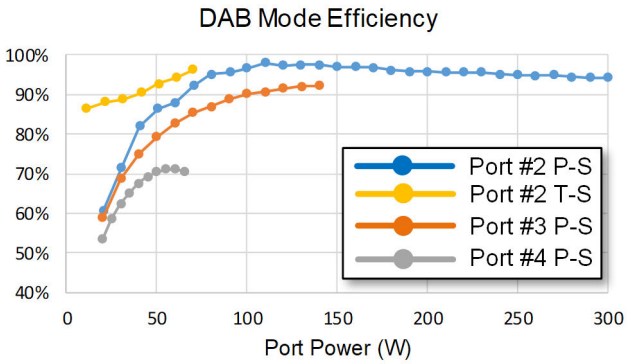

Fig. 18. Efficiency curves of 400V input DAB operation.

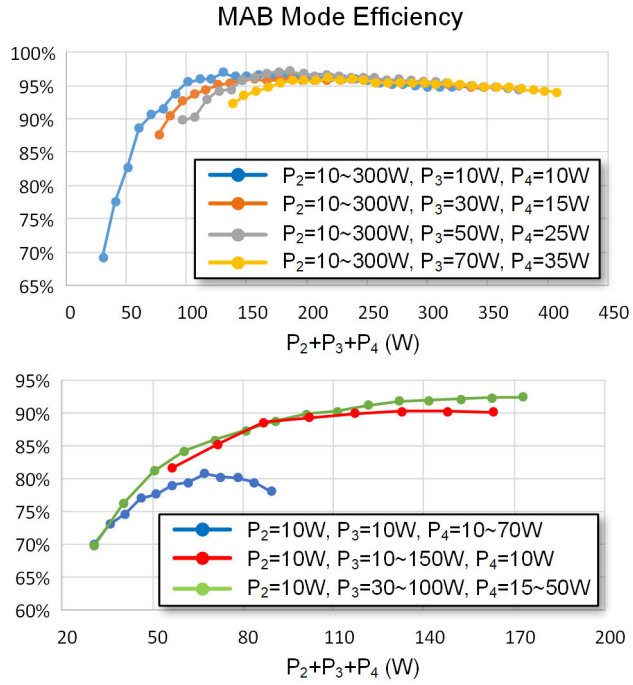

Fig. 19. Efficiency curves of 400V input MAB with phase-shift control.

the optimal power for time-sharing control. The efficiency of 400V-48V operation with time-sharing control in light load is also shown in Fig. 18, which is much higher than the efficiency with phase-shift control.

Fig. 19 shows the efficiency of the system with Port #1 as the input and Port #2–#4 as the output, all together. All ports are modulated with phase-shift control. The peak efficiency of the seven groups of test is 97.1% with 400V as the input and delivers 110W to 48V, 50W to 15V and 25W to 5V. The efficiency of the system drops significantly at light load.

Two instantaneous power cases are tested for time sharing control. Case 1 is [110 W, 140 W, 60 W] and Case 2 is [100 W, 100 W, 50 W] for Port #2–Port #4. Same instantaneous power setting is used in hybrid control for Port #3 and Port #4. Fig. 20 shows measured efficiency with the average power P_2 changes from 10 W to 300 W, and the average power of P_3 and P_4 both at 10W. Time-sharing control improves the

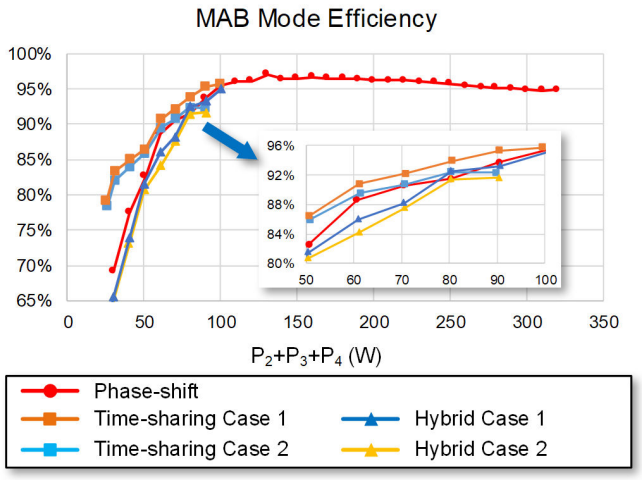

Fig. 20. Efficiency curves of 400 V input MAB operation with phase-shift, time-sharing and hybrid control, $P_2 = 10$ W-to-300 W, $P_3 = P_4 = 10$W.

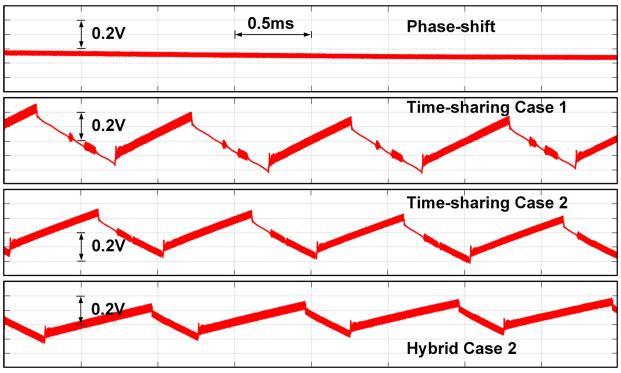

Fig. 21. Voltage ripple of Port #2 with phase-shift, time-sharing and hybrid control, $P_2 = 60$W, $P_3 = P_4 = 10$W.

TABLE II
SUMMARY OF POWER FLOW CONTROL METHODS

	Phase-shift	Time-sharing	Hybrid
Control Loops	coupled	uncoupled	uncoupled
Power Capability	high	lowest	low
Efficiency with Light Load	low	high	low
Voltage Ripple	lowest	highest	high

light load efficiency by 5%–15%.

Fig. 21 shows the voltage ripple of Port #2 under the three control methods. Both time-sharing control and hybrid control generate 1 kHz voltage ripple at the port.

Table II summarizes the advantages and tradeoffs of the phase-shift, time-sharing and hybrid control.

VIII. CONCLUSIONS

This paper presents three power flow control methods for MAB converters targeting low voltage dc power delivery in smart home applications. The phase-shift control has higher power capability and lower voltage ripple but the control loops are cross-coupled; the time-sharing control is easy to implement and more efficient at light load, but has lower device utilization ratio and higher voltage ripple; and the hybrid control can merge the advantage of the two methods and create mutual advantages. The small signal behaviors of the three control strategies are investigated in detail. The effectiveness of the three power flow control methods are verified by a 4-port MAB converter prototype.

ACKNOWLEDGMENT

The authors would like to thank the Siebel Energy Institite and the E-ffiliates program of Princeton University for supporting this work.

REFERENCES

[1] M. N. Kheraluwala, R. W. Gascoigne, D. M. Divan and E. D. Baumann, "Performance Characterization of a High-Power Dual Active Bridge dc-to-dc Converter," in *IEEE Transactions on Industry Applications*, vol. 28, no. 6, pp. 1294-1301, Nov/Dec 1992.

[2] R. W. A. A. De Doncker, D. M. Divan and M. H. Kheraluwala, "A Three-Phase Soft-Switched High-Power-Density dc/dc Converter for High-Power Applications," *IEEE Transactions on Industry Applications*, vol. 27, no. 1, pp. 63-73, Jan/Feb 1991.

[3] X. Liu, Z. Zheng, K. Wang and Y. Li, "An energy router based on multi-winding high-frequency transformer," *2016 IEEE Applied Power Electronics Conference and Exposition (APEC)*, Long Beach, CA, 2016, pp. 3317-3321.

[4] S. Falcones, R. Ayyanar, and X. Mao, "A dc–dc Multiport-Converter Based Solid-State Transformer Integrating Distributed Generation and Storage," *IEEE Transactions on Power Electronics*, vol. 28, no. 5, pp. 2192-2203, May 2013.

[5] J. Schäfer, D. Bortis and J. W. Kolar, "Multi-port multi-cell dc/dc converter topology for electric vehicle's power distribution networks," *2017 IEEE 18th Workshop on Control and Modeling for Power Electronics (COMPEL)*, Stanford, CA, 2017, pp. 1-9.

[6] M. Chen, M. Araghchini, K. K. Afridi, J. H. Lang, C. R. Sullivan and D. J. Perreault, "A Systematic Approach to Modeling Impedances and Current Distribution in Planar Magnetics," *IEEE Transactions on Power Electronics*, vol. 31, no. 1, pp. 560-580, Jan. 2016.

[7] M. Chen, K. K. Afridi, S. Chakraborty and D. J. Perreault, "Multitrack Power Conversion Architecture," in *IEEE Transactions on Power Electronics*, vol. 32, no. 1, pp. 325-340, Jan. 2017.

[8] M. Chen, S. Chakraborty and D. J. Perreault, "Multitrack Power Factor Correction Architecture," in *IEEE Transactions on Power Electronics*, early access.

[9] C. Zhao, S. D. Round and J. W. Kolar, "An Isolated Three-Port Bidirectional dc-dc Converter With Decoupled Power Flow Management," in *IEEE Transactions on Power Electronics*, vol. 23, no. 5, pp. 2443-2453, Sept. 2008.

[10] G. Buticchi, L. F. Costa, D. Barater, M. Liserre and E. D. Amarillo, "A Quadruple Active Bridge Converter for the Storage Integration on the More Electric Aircraft," in *IEEE Transactions on Power Electronics*, vol. 33, no. 9, pp. 8174-8186, Sept. 2018.

[11] P. Wang and M. Chen, "Towards Power FPGA: Architecture, Modeling and Control of Multiport Power Converters," *IEEE 19th Workshop on Control and Modeling for Power Electronics (COMPEL)*, Padova, 2018, pp. 1-8.

[12] M. Neubert, S. P. Engel, J. Gottschlich and R. W. De Doncker,"Dynamic power control of three-phase multiport active bridge dc-dc converters for interconnection of future dc-grids," *IEEE 12th International Conference on Power Electronics and Drive Systems (PEDS)*, Honolulu, HI, 2017, pp. 639-646.

[13] A. M. Imtiaz and F. H. Khan, "'Time Shared Flyback Converter' Based Regenerative Cell Balancing Technique for Series Connected Li-Ion Battery Strings," in *IEEE Transactions on Power Electronics*, vol. 28, no. 12, pp. 5960-5975, Dec. 2013.

[14] D. Maksimovic, R. W. Erickson and C. Griesbach, "Modeling of Cross-Regulation in Converters Containing Coupled Inductors," *IEEE Transactions on Power Electronics*, vol. 15, no. 4, pp. 607-615, Jul 2000.

[15] J. D. Glover, M. S. Sarma, and T. J. Overbye, *Power System Analysis and Design*, 4th ed. Toronto, ON, Canada: Thomson, 2008.

[16] R. D. Zimmerman, C. E. Murillo-Sanchez and R. J. Thomas, "MATPOWER: Steady-State Operations, Planning, and Analysis Tools for Power Systems Research and Education," *IEEE Transactions on Power Systems*, vol. 26, no. 1, pp. 12-19, Feb. 2011.